APS physics

CHORUS

This is the accepted manuscript made available via CHORUS. The article has been published as:

# Optical and transport measurement and first-principles determination of the ScN band gap

Ruopeng Deng, B. D. Ozsdolay, P. Y. Zheng, S. V. Khare, and D. Gall

Phys. Rev. B **91**, 045104 — Published 6 January 2015

DOI: 10.1103/PhysRevB.91.045104

# The ScN Bandgap

Ruopeng Deng,[1] B.D. Ozsdolay,[1] P.Y. Zheng,[1] S.V. Khare[2] and D. Gall[1]
[1]*Department of Materials Science and Engineering, Rensselaer Polytechnic Institute, Troy, New York 12180, USA*
[2]*Department of Physics and Astronomy, University of Toledo, 2801 West Bancroft Street, Toledo, OH 43606*

The electronic structure of scandium nitride is determined by combining results from optical and electronic transport measurements with first-principles calculations. Hybrid functional (HSE06) calculations indicate a 0.92 eV indirect Γ-to-X band gap and direct transition energies of 2.02 and 3.75 eV at Γ- and X-points, respectively, while $G_oW_o$ and $GW_o$ methods suggest 0.44-0.74 eV higher gap values. Epitaxial ScN(001) layers deposited on MgO(001) substrates by reactive sputtering exhibit degenerate n-type semiconductor properties with a temperature-independent electron density that is varied from $N = 1.12\text{-}12.8\times10^{20}$ cm$^{-3}$ using F impurity doping. The direct optical gap increases linearly with $N$ from 2.18 to 2.70 eV, due to a Burstein-Moss effect. This strong dependence on $N$ is likely the cause for the large range (2.03-3.2 eV) of previously reported gap values. However, here extrapolation to $N = 0$ yields 2.07±0.05 eV for the direct X-point transition of intrinsic ScN. A reflection peak at 3.80±0.02 eV is independent of $N$ and in perfect agreement with the HSE06-predicted peak at 3.79 eV, associated with a high joint-density of states near the Γ-point. The electron mobility at 4 K is 100±30 cm$^2$/Vs and decreases with temperature due to scattering at polar optical phonons with characteristic frequencies that decrease from 620 to 440±30 cm$^{-1}$ with increasing $N$, due to free carrier screening. The transport and density-of-states electron effective mass, determined from measured intra and inter band transitions, respectively, are 0.40±0.02 $m_o$ and 0.33±0.02 $m_o$, in good agreement with the first-principles predictions of $m_{tr}$ = 0.33±0.05 $m_o$ and $m_{DOS}$ = 0.43±0.05 $m_o$. The ScN refractive index increases with increasing hν = 1.0-2.0 eV from 2.6-3.1 based on optical measurements and from 2.8-3.2 based on the calculated dielectric function. An overall comparison of experiment and simulation indicates (i) an overestimation of band gaps by GW methods but (ii) excellent agreement with a deviation of ≤0.05 eV for the hybrid functional and (iii) a value for the fundamental indirect gap of ScN of 0.92±0.05 eV.

## I. INTRODUCTION

Scandium Nitride (ScN) is a rock-salt structure nitride with a high melting point[1] and hardness,[2-4] and great potential as buffer or interface layer[5-8] or alloy material with GaN,[9-11] AlN,[12-21] SiC,[5] and MnN[22-26] to form new optoelectronic,[10, 11, 14] piezoelectric,[13, 15-18, 27] spintronic[23-25] or thermoelectric[26, 28-31] materials. Despite the great interest in ScN, its electronic structure and particularly the value of its bandgap are not well known. Early work on ScN was very controversial, with conclusions from both experimental and theoretical work ranging from ScN being a semimetal with a 0.0-0.2 eV band overlap[32-34] to ScN being a semiconductor with a band gap >2 eV.[35-43] During the last decade, consensus has been reached that ScN is a semiconductor with an indirect gap from the valence band at the Brillouin zone center (Γ-point) to the conduction band at the X-point, and a lowest-energy direct transition at the X-point. Optical absorption measurements from ScN layers deposited by reactive evaporation,[34, 40, 44] reactive sputtering,[26, 41, 42, 45] molecular beam epitaxy,[43, 46, 47] and chemical vapor deposition,[37] yield values for this latter direct transition ranging from 2.03 to 3.2 eV. [2, 26, 34, 37, 40, 42-48] This large range of reported optical band gaps in ScN is attributed to nitrogen vacancies,[29] and oxygen,[26, 45] halide,[37] or other impurities,[29] that lead to relatively large carrier concentrations reported to range from $5\times10^{16}$ to $10^{22}$ $cm^{-3}$.[26, 34, 37, 42, 43, 45-52] and cause a Burstein-Moss shift that increases the observed band gap[45, 53] and/or conversely cause band tails that decrease the observed band gap. The fundamental indirect band gap in ScN is rarely measured experimentally. The only reports are from a combination of tunneling spectroscopy and optical absorption, suggesting a value of 0.9±0.1,[46] from photoelectron spectroscopy, providing a value of 1.3±0.3,[42] from reflection electron energy loss spectroscopy yielding 1.5±0.3,[52] and from extrapolating optical absorption suggesting 0.9-1.2 eV,[26] depending on how oxygen impurities are accounted for. Early density functional calculations on the electronic structure of ScN suggest a band overlap between the Γ-point valence band top and the X-point conduction band bottom.[32-34] However, more recent theoretical results with improved exchange correlation functionals predict a direct X-point transition of 1.82-2.59 eV and an indirect band gap of 0.79-1.70 eV.[29, 42, 54-62] These values are consistent with the experimental ranges of 2.03-3.2 eV and

0.9-1.5 eV for the direct and indirect transitions, respectively. However, the large ranges for gap values from both experimental and theoretical studies are unsatisfactory and motivate the present investigation.

In this article, we present results from a combined experimental and theoretical study with the primary goal to provide more reliable values for the band gap energies of ScN. The novelty on the experimental side is to measure gap values as a function of carrier concentration $N$ and to determine the "true" band gap of ScN by extrapolating to a zero carrier concentration. This approach is used because impurities and nitrogen vacancies in combination with the associated free carrier concentration are believed to lead to the large range of reported gap values. Thus, by systematically studying the correlation between carrier concentration and gap values, we remove the ambiguity associated with the different ScN synthesis methods employed in the various reported studies. On the computational side, we use both hybrid-exchange correlation functional and GW calculations. These methods have been shown to dramatically improve the accuracy of predicted gap values for a large range of semiconductors in comparison to the conventional local density or generalized gradient approximations.[63-65] In addition, the calculated band structure is used to predict the ScN optical properties which are directly compared to the experimental spectra, providing a method to check the accuracy of the calculated electronic structure and to quantify the interband spacing based on optical transitions well above the direct gap. This quantitative comparison is particularly important to relate a calculated high joint-density of states due to a set of parallel bands to a peak in the measured optical reflection that is related to a feature in the ScN dielectric function at 3.8 eV. We find that the band structure calculated with a hybrid exchange correlation functional predicts optical properties that agree within ±0.05 eV with the measured optical properties of ScN layers extrapolated to $N = 0$, while $G_oW_o$ and $GW_o$ calculations overestimate band gaps by 0.4-0.7 eV. Single crystal ScN(001) layers are deposited by reactive sputtering on MgO(001) substrates and their carrier concentration is varied from $N = 1.12$ to $12.8\times10^{20}$ cm$^{-3}$ using F impurities. The measured optical properties are independent of the N-vacancy concentration, the crystalline quality, and the intrinsic strain, but are affected by $N$. In

particular, increasing $N$ causes an increase in the apparent band gap associated with the lowest energy direct transition at the X-point, due to a Burstein-Moss effect, while a feature in the reflection spectrum at a higher energy is unaffected by $N$, indicating negligible band-to-band shifts associated with the F doping, justifying direct extrapolation of transition energies to $N = 0$. This yields an experimental value for the direct transition at the X-point of 2.07±0.05 eV, while the feature in the reflection spectra associated with a high joint density of states is at 3.80±0.02 eV. These values are in excellent agreement with our first-principles predictions of 2.02 and 3.79 eV, indicating that the electronic structure calculation using the HSE06 functional provides accurate gaps for ScN, such that the predicted fundamental indirect gap of 0.92 eV is also expected to be accurate, with an estimated uncertainty of ±0.05 eV. In addition, there is also excellent quantitative agreement between experiment and simulation for the values of the electron effective masses and the refractive index vs wavelength, confirming the accuracy of the calculated band structure.

## II. PROCEDURE

### A. Sample Preparation and Analysis

Epitaxial ScN layers were deposited by reactive magnetron sputtering in a load-locked ultra-high vacuum deposition system with a base pressure of $10^{-9}$ Torr. Double-side polished 10×10×0.5 $mm^3$ magnesium oxide MgO(001) substrates were ultrasonically cleaned in trichloroethylene, acetone and isopropyl alcohol for 15 min each, rinsed in de-ionized water, blown dry with dry nitrogen, mounted onto a substrate holder using silver paint, inserted into the deposition system, and degassed for 1 hour at 1000 °C.[14, 66] Prior to deposition, the 5-cm-diameter nominally 99.99% pure Sc target was sputter-cleaned for 10 min in a 99.999% pure $N_2$/Ar gas using a protective disc preventing the deposition flux reaching the substrate. Deposition was initiated by removing the disc and lowering the substrate temperature to 850 or 950 °C, as measured with a pyrometer that was cross-calibrated by a thermocouple underneath the substrate holder. The substrate was continuously rotated at 60 rpm to ensure layer thickness uniformity. A total of 19 ScN samples were deposited in order to explore how

the structural and electronic properties of ScN may be affected by various deposition parameters, including the power (60-300 W) to the Sc target, the total gas pressure (5 and 20 mTorr), the $Ar/N_2$ partial pressure ratio (0 and 0.25), the substrate temperature (850 and 950°C), and the substrate bias (0 to -50 V). The deposition time (20-220 min) was adjusted for each sample, to yield comparable ScN film thicknesses ranging from 180-350 nm, as measured by cross-sectional scanning electron microscopy, using a Carl Zeiss Supra microscope.

UV-to-Visible (UV-Vis) transmittance *T* and reflectance *R* spectra were acquired in a Perkin-Elmer Lambda 950 spectrophotometer over a wavelength range from 200-3000 nm in 1 nm steps. The reflectance spectra were obtained from a 6° incident angle and were calibrated using an Al mirror reference which was cross-calibrated with the polished surface of a sapphire substrate and optical constants of sapphire from Palik's handbook.[67] The refractive index and extinction coefficient of the MgO substrates as a function of wavelength were determined from *R* and *T* spectra of double-side polished 0.5 mm thick substrates considering an infinite set of incoherent internal reflections. The obtained values agree well with the reported refractive index[67] for the investigated wavelength range, with a maximum deviation of 3%. The spectra from the ScN layers were analyzed by accounting for interference effects associated with reflections at the air/ScN and the ScN/MgO interfaces using O. S. Heaven's formulas,[68] and treating absorption in the substrate and the multiple light paths associated with reflection at the backside of the substrate by incoherent addition. All data analyses assumed normal incident light for reflection instead of the experimental 6°, which causes negligible (<1%) errors in the presented data.

The room-temperature resistivity was determined using a linear four point probe. The values were confirmed using an Accent HL5500 Hall system with a 0.518 T magnetic field which was also utilized to measure the free carrier concentration using a van der Pauw geometry. The temperature-dependent resistivity was measured in vacuum in a Cryo-magnetics Inc. $^4$He cryostat system during warm-up from 4-300 K. For this purpose, 1.5×1.5 $mm^2$ Al, Cu or Au contacts were sputter deposited on the corners of each sample to form a van der Pauw geometry which was contacted with silver paint

to the wire leads. For each sample, resistances $R_{12\text{-}34}$, $R_{34\text{-}12}$, $R_{14\text{-}32}$, and $R_{32\text{-}14}$ in both current directions were measured at room temperature and 4 K to accurately solve for the sheet resistance $R_s$.[69] The geometric correction factor $R_{12\text{-}34}/R_s$ for the two temperatures was in agreement (<3%) for all samples and was used to determine the temperature dependence of $R_s$ from $T$ = 4-300 K from the measured $R_{12\text{-}34}(T)$. All ScN films were sufficiently resistive such that the thermoelectric voltage offset at zero current was much less (<1%) than the voltage drop across the layer at measurement current, which was also chosen to be small enough to have no detectable heating effect. The film resistivity $\rho$ was determined from the measured $R_s$ and the layer thickness.

**B. Composition, Structure, and Carrier Concentration**

In this subsection, we present and discuss the compositional and structural analysis of the 19 ScN samples that were deposited at various deposition conditions. This careful analysis is primarily motivated by the large variation in previously reported ScN band gap values which we attribute to either compositional and/or structural differences between the samples from different researchers. In summary we find that (i) deposition conditions including the deposition power, processing gas composition and pressure, substrate temperature, and the ion flux energy affect the crystalline quality, the strain level, and also the nitrogen-vacancy concentration, but have negligible effect on the carrier concentration and, in turn, on the measured optical band gaps; and (ii) the carrier concentration in the deposited ScN layers is primarily determined by impurities from the Sc target. More specifically, a tantalum impurity of 0.04±0.01 at.% which remains constant for all ScN layers, and a fluorine (F) impurity which decreases over the lifetime of the Sc target, leading to F in the ScN which decreases from 3±1 to <0.5 at.%, with a related decrease in $N$ from 12.8 to $1.12\times10^{20}$ cm$^{-3}$. Here and throughout the paper, $N$ refers to the carrier concentration as measured by room temperature Hall measurements. Setting the carrier concentration equal to the result from the Hall measurement is accurate within an estimated systematic error of ~10%, and is justified, based on optical and transport measurements presented in the following sections, which show that all layers are purely n-type, have a carrier

concentration with negligible temperature dependence, and a Hall factor close to unity. The remainder of this section contains a detailed description of the compositional and structural results, which support the finding that the main parameter distinguishing the samples in this study is the carrier concentration, which is primarily controlled by F doping.

ScN layer compositions were determined using a combination of x-ray photoelectron spectroscopy (XPS), Auger electron spectroscopy (AES), and Rutherford backscattering spectroscopy (RBS). XPS and AES spectra were acquired using a PHI 5000 VersaProbe and a ULVAC-PHI 700. Measurements were performed both before and after sputter etching with a 1000 eV $Ar^+$ beam to remove surface contaminants like adsorbed $H_2O$ and hydrocarbons as well as surface oxides which cause errors in the absolute composition values. However, the sputter cleaning procedure also introduces errors as it causes preferential sputtering of light elements, leading for example to a 10-15% change in the measured N:Sc ratio,[70] and is therefore not suited for exact quantitative composition determination. Consequently, XPS and AES measurements are primarily used to semi-quantitatively detect light-element impurities. More specifically, both XPS and AES indicate a considerable concentration of F impurities in the ScN layers. The F concentration shows no detectable correlation with deposition parameters but decreases with increasing sample number from, for example, 3±1 and 2.0±0.2 at.% for samples #28 and #29 to 0.8±0.2, 0.2±0.1, and 0.7±0.2 at.% for samples #38, #39, and #41, and is below the detection limit for sample #47. We attribute the F in our ScN layers to stem from target impurities which are due to the Sc purification process by fluoride reduction.[71] The purification of rare earth elements is known to lead to considerable non-metallic impurity concentrations, even if the nominal purity is 99.99%.[71] The decrease of F over the lifetime of the Sc target and, in turn, the variation in the F concentration in the deposited ScN layers, is attributed to continued outgassing of the F in the Sc target during temperature cycling associated with sputter deposition, sample degassing, and chamber baking. In parallel with the decreasing F concentration, the measured carrier concentration also decreases over the Sc target lifetime, strongly suggesting that F acts as a donor in ScN, as

expected for substitutional F impurities on N-sites and consistent with reported first-principles simulation results.[29]

RBS spectra were obtained using 2 MeV $^4He^+$ ions incident at an angle of 6° relative to the surface normal with the detector set at a 166° scattering angle. The compositional analysis by RBS is complementary to XPS and AES, as it does not require a surface cleaning procedure and is therefore suitable to determine the N:Sc ratio. However, due to the low scattering cross-section for light elements, the values contain a relatively large uncertainty. In particular, RBS show N:Sc ratios ranging from 0.90±0.03 to 0.97±0.03, suggesting compositions that range from N-deficient to nearly stoichiometric within experimental uncertainty. The lowest nitrogen concentrations are found for samples deposited at high temperature $T_s$ = 950 °C, suggesting that temperature activated desorption may cause N deficiency in ScN, similar to what has been reported for CrN,[72] TaN,[73] and HfN.[74] The measured nitrogen deficiency corresponds to N vacancy concentrations $N_v$ ranging from $1\pm1\times10^{21}$ to $4\pm1\times10^{21}$ cm$^{-3}$. The sample-to-sample variation in $N_v$ has no detectable effect on the optical properties presented in the next section. Also, there is no detectable correlation between $N_v$ and the measured carrier concentration, indicating that N vacancies do not provide charge carriers to the conduction band. This is in contradiction to previous reports, suggesting that the carrier concentration may be due to N vacancies,[26, 43, 46] but is consistent with recent first principles calculations, indicating that N vacancies cause deep-level defect states within the ScN band gap.[29]

RBS spectra also indicate a Ta impurity of 0.04±0.01 at.% in all measured ScN layers. This corresponds to a Ta concentration of $3.5\pm0.9\times10^{19}$ cm$^{-3}$. The Ta is attributed to stem from the Sc metal source, since Ta is the common crucible material used in the reactor for rare earth purification, and is therefore a common impurity in purified rare earth elements.[71] Substitutional Ta impurities on Sc-sites may act as donors in ScN and may be responsible for the residual carrier concentration for samples where no F impurity could be detected. However, our experimental detection limit for F is $4\times10^{20}$ cm$^{-3}$ cm$^{-3}$. Thus, the origin for the charge carriers for samples with low $N < 4\times10^{20}$ cm$^{-3}$ cannot be uniquely determined, and is likely due to a combination of F and/or Ta impurities but could also be affected by

residual N-vacancy effects or other impurities with concentrations below the detection limit. In summary, the large range of carrier concentration $N = 1.12\text{-}12.8\times10^{20}$ cm$^{-3}$ in our ScN layers is due to the varying F impurity concentration, while the nitrogen vacancy concentration and Ta impurities have negligible effect on $N$.

Extensive x-ray diffraction (XRD) analyses were performed on all samples, in order to confirm epitaxy, measure strain, and quantify crystalline quality. XRD $\omega$-$2\theta$ spectra were collected in a PANalytical X'Pert Pro diffractometer over a $2\theta$ range from 33-75°, using a hybrid x-ray mirror containing a two-crystal monochromator yielding Cu $K\alpha_1$ radiation (1.5406 Å) with a 0.0068° divergence, and using a 0.27°-acceptance parallel plate collimator in front of a scintillator point detector. The crystalline mosaicity of the layers was measured using $\omega$-rocking-curve scans of the ScN 002 reflection, using a diffractometer setup with an x-ray mirror but without a monochromator. The cube-on-cube epitaxial relationship of the ScN(001) layers with the MgO(001) substrates was confirmed by phi scans at constant $2\theta$ values corresponding to the ScN 222 and MgO 222 reflections, using the same x-ray optics as for $\omega$ rocking curve scans. Typical XRD results from a 262-nm-thick ScN(001) layer are included as supplemental material.[75] The following paragraph is a summary of the findings from the XRD analyses.

All ScN layers are epitaxial single crystals, as determined with a combination of XRD $\omega$-$2\theta$, ScN 002 $\omega$-rocking-curve, and ScN 222 □-scans. Their degree of strain and crystalline quality are affected by deposition conditions. In particular, the magnitude of compressive strain is most strongly affected by the substrate bias $U_s$. For example, the strain increases from 0.47% to 0.48%, 0.54%, 0.80% for $U_s$ = 0, -12, -20, -30 V, using a constant $T_s$ = 950 °C, 5 mTorr $N_2$, and $p_{Sc}$ = 180 W. The strain also increases with increasing power to the magnetron deposition source, from 0.55% to 0.64%, 1.1%, 1.6% with $p_{Sc}$ = 60, 180, 240, 300 W at a constant $T_s$ = 950 °C, 5 mTorr $N_2$, and a floating substrate potential. With increasing stress, the crystalline quality decreases, as evidenced by the x-ray $\omega$-rocking-curve width which ranges from 0.61° to 3.7° for all samples in this study. In contrast, substrate temperature and processing gas mixture and pressure have no detectable effect on strain or crystalline quality. Also,

all deposition parameters and related microstructural changes including strain and crystalline quality have no detectable effect on the optical properties presented in the next section.

### C. Computational Approach

All density functional theory (DFT) calculations were performed using the Vienna *ab initio* simulation package (VASP), employing periodic boundary conditions, a plane wave basis set, and the projector-augmented wave (PAW) method.[76] Initial calculations were done using the Perdew-Burke-Ernzerhof (PBE) generalized gradient approximation exchange correlation functional,[77] followed by calculations with the HSE06 hybrid functional with the short range exchange energy corresponding to the sum of 25% of the exact exchange and 75% of the PBE exchange, while the correlation energy and the long-range part of the exchange energy are kept fixed at the PBE values.[78] A 25% mixing is considered optimal for ScN, based on a comparative study of hybrid functionals.[59] Thirdly, GW calculations[63] are performed using PAW potentials that are optimized to obtain accurate excited state energies,[79] and keeping the wavefunctions fixed as those obtained from the DFT calculations with the HSE06 functional. We refer to single shot calculations as $G_oW_o$, and calculations where eigenvalues in the Green's function G are updated to reach self-consistency as $GW_o$, while eigenvalues of the dielectric matrix of the screened potential W remain fixed.[80]

All computational parameters are chosen such that the presented gap energies are converged to within 0.01 eV. This includes a 500 eV cut-off energy for the plane-wave basis set expansion, a 10×10×10 k-point grid which includes the Γ- and X-points to sample the Brillouin zone of the primitive 2-atom unit cell, and 1000 frequency points along the real axis for the GW calculations. The Sc 3*s* and 3*p* electrons are explicitly calculated, i.e. they are not included in the core of the potential. Polynomial fitting of the total energy vs lattice constant yields minima at 4.519±0.003 and 4.499±0.002 Å for the conventional PBE and the hybrid HSE functionals, respectively. The former is 0.4% larger than the reported experimental room-temperature ScN lattice constant of 4.501±0.002 Å,[81] consistent with the typical overestimation of lattice constants for the generalized gradient

approximation.[65] In contrast, the value using the HSE functional is in perfect agreement with the experimental value, considering the 0.05% experimental and computational uncertainties. In the following, all calculated values presented in this report are obtained using a lattice constant of 4.50 Å.

The optical properties are determined from the electronic structure following the method described in Ref. 82, using the VASP simulation package. The complex dielectric function $\varepsilon = \varepsilon_1 + i\varepsilon_2$ vs photon energy is obtained by first determining $\varepsilon_2$ by summation over filled and empty states, followed by a Kramers-Kronig transformation which yields $\varepsilon_1$. These calculations are done using 20,000 frequency points corresponding to a 0.01 eV energy spacing, a complex shift of 0.01 eV for the Kramers-Kronig transformation, and the HSE06 functional with a total of 24 bands yielding empty states up to 40 eV above the Fermi level. This results in converged values for $\varepsilon_1$ and $\varepsilon_2$ with a computational uncertainty of ±0.2 over the entire reported 0-6 eV energy range. Convergence of optical properties with respect to the *k*-point mesh is challenging, as convergence is much slower than for the band gap values. In particular: band gaps are converged to ±0.01 eV for 6×6×6 and 8×8×8 *k*-points for the hybrid functional and the GW calculations, respectively, and are reported in this paper for calculations using a 10×10×10 mesh. In contrast, the primary peak in $\varepsilon_2$ near $h\nu = 4$ eV is sensitive to the *k*-point mesh. For example, it shifts by -0.12 eV as the number of *k*-points is increased from 14×14×14 to 18×18×18, indicating that convergence is not reached for a 18×18×18 mesh. Similarly, the slope $d\varepsilon_2/d(h\nu)$ above the onset for direct interband transitions increases from 7.0 to 9.0 $(eV)^{-1}$ as the mesh is increased from 14×14×14 to 18×18×18. This slow convergence is a considerable challenge due to the high computational cost of hybrid functional calculations, but has been resolved in this study by calculating the short-range Fock contribution on a relatively coarse 8×8×8 *k*-space grid while the other contributions to the Hamiltonian are determined on a finer 48×48×48 mesh. Careful testing shows that the positions of the relevant features in $\varepsilon$ are converged to within 0.02 eV for this choice of *k*-point meshes.

## III. RESULTS AND DISCUSSION

Figure 1(a) shows the band structure of rock-salt ScN along high symmetry directions in the Brillouin zone, as obtained from density functional calculations using the HSE06 hybrid exchange correlation functional.[78] The energy scale is set such that the Fermi-level ($E_F$ = 0) is at the top of the valence band, which is 5.60 eV wide and consists of three bands that exhibit primarily N 2*p* character. The N 2*s* band is 13.59-15.75 eV below $E_F$, and the Sc 3*p* bands (not shown) are at $E$ = -29.59 to -28.87 eV. The six plotted conduction bands range from 1-14 eV, exhibit primarily Sc 3*d*-4*s* character, and have their highest density of states at 6.2-7.2 eV above $E_F$.

The calculated band structure shows that ScN is a semiconductor with a predicted 0.92 eV indirect bandgap from the valence band maximum at the zone center (Γ) to the conduction band minimum at the X-point. The lowest energy direct transition between valence and conduction band is at the X-point and has a value of 2.02 eV, while the direct transition at the Γ-point is 3.75 eV. Corresponding calculations using the PBE GGA functional (not shown) considerably underestimate gap values, as expected for conventional exchange correlation functionals,[63] with a predicted small Γ-X band overlap of 0.04 eV, and X-X and Γ-Γ transition energies of 0.88 and 2.42 eV, in agreement with early band structure calculations for ScN.[32-34] Additional $G_oW_o$ and $GW_o$ calculations which build on the electronic structure calculated with the hybrid functional yield values for the indirect Γ-X gap of 1.37 and 1.43 eV, respectively, while the direct transitions are 2.46 and 2.52 eV at the X-point, and 4.39 and 4.49 eV at the Γ-point, respectively. These values are considerably larger than what is obtained using the HSE06 functional. In particular, the single shot $G_oW_o$ approach raises the gap values by 0.45, 0.44, and 0.64 eV, respectively, while selfconsistency in G slightly increases the values by an additional 0.06-0.10 eV above the $G_oW_o$ gaps. This is consistent with systematic comparative studies on a range of known semiconductors, which find that fundamental predicted gaps using $G_oW_o$ are 25-45% larger than those obtained with the HSE03 functional,[83] and that $GW_o$ gaps are in average just 6% larger than $G_oW_o$ gaps,[80] and that this difference decreases to 3% if the starting wavefunctions are obtained using hybrid rather than conventional functionals.[83] We note here that the HSE06 functional, which is used in this study and uses a screening parameter $\omega$ = 0.207 $Å^{-1}$, yields larger and

typically more accurate gap values than the HSE03 functional ($\omega$ = 0.3 Å$^{-1}$) used in the above studies.[84] In fact, comparing the simulated and experimental optical response of ScN, as discussed below, indicates that the calculation with the HSE06 functional provides correct (±0.05 eV) gap values while the $G_oW_o$ and $GW_o$ calculations overestimate ScN band gaps. A similar (but typically smaller) band gap overestimation by GW approaches has been reported for most semiconductors including Ge, Si, GaAs, SiC, CdS, AlP, GaN.[83]

The electron effective mass is predicted using a parabolic approximation to the calculated conduction band shape at the X-point. The longitudinal effective mass $m_l$ along the X→Γ direction is found to be 1.44±0.02 $m_o$, where $m_o$ is the free electron mass, while the transverse effective mass $m_t$ = 0.24±0.04 $m_o$ along the X→W direction (not shown) is six times smaller than $m_l$. The transport effective mass $m_{tr}$ for n-type carriers is then determined using $\frac{3}{m_{tr}} = \frac{1}{m_l} + \frac{2}{m_t}$ which is based on an ellipsoid approximation of the Fermi surface, yielding $m_{tr}$ = 0.33±0.05 $m_o$. This value is close to the experimental result of $m_{tr}$ = 0.40±0.02 $m_o$ presented below, and is within the (rather large) range from 0.18 to 0.39 to 1.07 of previously reported first-principles predictions of the ScN effective mass.[57, 60, 85] Similarly, the density-of-states effective mass $m_{DOS}$ is obtained using $m_{DOS}^3 = m_l m_t^2$.[86] This yields a predicted $m_{DOS}$ = 0.43±0.05 $m_o$, which is slightly larger than the experimental $m_{DOS}$ = 0.33±0.02 $m_o$ presented below.

Figure 1(b) is a plot of the predicted real and imaginary part of dielectric function $\varepsilon = \varepsilon_1 + i\varepsilon_2$ vs photon energy h$\nu$ = 0-5.5 eV, as calculated from the electronic structure obtained using the HSE06 functional. The $\varepsilon_1$ curve increases from 7.7 at low photon energies to a maximum of $\varepsilon_1$ = 11.7 at 2.09 eV, followed by a gradual decrease with minor peaks of $\varepsilon_1$ = 8.0 at 3.76 eV and $\varepsilon_1$ = 6.0 at 5.00 eV to reach 5.4 at h$\nu$ = 6 eV. The $\varepsilon_2$ curve is zero below the onset of direct interband transitions, increases steeply for h$\nu$ > 2.0 eV to reach $\varepsilon_2$ = 4.0 at 2.6 eV, continues to rise to a maximum of $\varepsilon_2$ = 6.3 at 3.80 eV, decreases nearly linearly to a minimum of $\varepsilon_2$ = 4.4 at 4.95 eV, and increases to 5.3 at h$\nu$ = 6 eV. The complete data set for h$\nu$ = 0-10 eV is included as supplemental material.[75]

The steep increase in $\varepsilon_2$ above h$\nu$ = 2.0 eV and the corresponding peak in $\varepsilon_1$ at 2.09 eV are due to the onset of direct interband transitions at the X-point, with a predicted gap of 2.02 eV. The peak in $\varepsilon_2$ at 3.80 eV and the related drop in $\varepsilon_1$ are due to a high joint-density of states associated with nearly parallel bands near the Γ-point. This peak does not exactly correspond to the direct transition at the Γ-point, which has a 0.05 eV lower energy of 3.75 eV, but to transitions from the three highest valence bands (of which two are degenerate along Γ-X) to the lowest conduction band which are nearly parallel in a region around a point that is slightly offset from Γ along the Γ-X direction.

Figure 2 shows optical reflectance $R$ and transmittance $T$ spectra from three representative ScN samples with $N = 1.12\times10^{20}$, $5.10\times10^{20}$, and $8.56\times10^{20}$ cm$^{-3}$ and thickness of 262, 192, and 198 nm, respectively, as well as a simulated reflectance spectrum for pure (carrier-free) bulk ScN obtained from the calculated dielectric function shown in Fig. 1(b). The spectra from data fitting are plotted as dashed lines. The $R$ spectrum for $N = 1.12\times10^{20}$ cm$^{-3}$ in Fig. 2(a) exhibits strong interference fringes at photon energies ranging from h$\nu$ = 0.5 eV to the onset of strong absorption near 2 eV, indicating transparency in this energy range. The spectra with $N = 5.10\times10^{20}$ and $8.56\times10^{20}$ cm$^{-3}$ exhibit similar fringes, however, the fringes extend to higher photon energies, indicating that the interband transition energy increases with $N$. In addition, the fringe amplitude diminishes with decreasing photon energy and the reflection at h$\nu$ = 0.5 eV increases with $N$, due to free carrier intraband transitions. These trends are more pronounced in the corresponding transmittance spectra in Fig. 2(b), showing that increasing $N$ leads to a decrease in $T$ for h$\nu$ < 1 eV but an increase for h$\nu$ > 2 eV. The decrease at low h$\nu$ is attributed to an increasing plasma frequency with increasing $N$, such that the free carriers for $N$ larger than ~$5\times10^{20}$ cm$^{-3}$ cause considerable metallic reflection and absorption at h$\nu$ = 0.5 eV. The steep decrease in $T$ for h$\nu$ > 2 eV is attributed to the onset for interband transitions at the X-point, as discussed above. The transmission edge (arbitrarily defined as $T$ = 0.001) is 2.3 eV for $N = 1.12\times10^{20}$ cm$^{-3}$, but shifts to 2.6 and 2.7 eV for $N = 5.10\times10^{20}$ and $8.56\times10^{20}$ cm$^{-3}$, respectively. This is attributed to the Burstein-Moss effect, as discussed in more detail below, indicating that the free carriers occupy

states at the conduction band bottom at the X-point of the Brillouin zone, preventing interband transitions into these states.[53]

For h$\nu \geq 3$ eV, transmission is negligible and hence the reflectance spectra in Fig. 2(a) correspond to infinitely thick ScN specimens. Therefore, the measured $R$ for h$\nu \geq 3$ eV can be directly compared to the calculated spectrum. There is good agreement, both qualitatively and quantitatively between the measured and the predicted spectra. For example, the calculated $R$ at 3 and 6 eV is 0.28 and 0.26, which is in perfect agreement with the experimental values, which are 0.27-0.29 at 3 eV and 0.24-0.26 at 6 eV. More importantly, there is a simulated reflection peak at 3.79 eV, which is due to a $\varepsilon_2$ peak at 3.80 eV as shown in Fig. 1(b), and is associated with a high joint density of states near the Γ-point. This peak is clearly visible in the measured reflectance spectra and occurs for all ScN samples at the same photon energy of 3.80±0.02 eV. This suggests that the carrier density as well as other sample variations including crystalline quality, strain level, and density of N-vacancies and F impurities, have negligible effect on the interband transitions near the Γ point. The absence of a Burstein-Moss effect for these transitions indicates negligible charge carriers at the Γ point. That is, the hole concentration at the top of the valence band which occurs at the Γ point is negligible, consistent with the electron transport measurements and the optical data for the X-point transition, which both indicate that the charge carriers are n-type and that the Fermi level is near the bottom of the conduction band. The fact that the feature in the reflection spectra at 3.80±0.02 eV is independent of $N$ indicates that the spacing between valence and conduction bands is unaffected by the charge carrier density. Therefore, we can directly extrapolate the measured data as a function of $N$ to determine properties of intrinsic ScN with $N = 0$. More specifically, we expect perfect intrinsic ScN to also exhibit a peak in the reflection spectrum at 3.80±0.02 eV, in perfect agreement with the simulated reflection peak at 3.79 eV. Similarly, as discussed in detail below, we use extrapolation to $N = 0$ of the measured optical absorption onset to determine the X-point direct gap energy for intrinsic ScN.

The optical $R$ and $T$ spectra are analyzed using a Drude-Lorentz model for the wavelength range where the samples are partially transparent, which is defined as the wavelength range from the

near infrared (h$\nu$ = 0.5 eV) to the position of the interference fringe maximum closest to the onset of strong absorption, corresponding to 550, 540 and 532 nm for $N = 1.12\times10^{20}$, $5.10\times10^{20}$, and $8.56\times10^{20}$ cm$^{-3}$, respectively. The complex dielectric function $\varepsilon(\omega)$ is described by:[49]

$$\varepsilon(\omega) = \varepsilon_\infty - \frac{\omega_P^2}{\omega^2 + i\gamma_D\omega} + \frac{f_L}{\omega_L^2 - \omega^2 - i\gamma_L\omega} \quad , \tag{1}$$

where the onset of interband transitions is modeled with a Lorentz oscillator with a strength $f_L$, a frequency $\omega_L$, and damping factor $\gamma_L$. Higher energy transitions are accounted for by $\varepsilon_\infty$, which is the dielectric constant for energies well above the investigated range and the free carrier contribution is described with a classical Drude term where the free carrier damping term $\gamma_D$ corresponds to the inverse of the carrier relaxation time and the plasma frequency $\omega_P$ is given by:

$$\omega_P = \sqrt{\frac{e^2}{\varepsilon_0}\frac{N}{m_{tr}}} \, . \tag{2}$$

Here $e$ is the elementary charge, $\varepsilon_0$ the vacuum permittivity, $m_{tr}$ the transport effective mass, and $N$ the carrier concentration from the Hall measurements. The measured $R$ and $T$ spectra are simultaneously fitted for each sample with Eq. (1), and the resulting curves plotted as dashed lines in Figs. 2(a) and (b). There is excellent quantitative agreement between fitted and measured curves, indicating the ScN optical properties are well described by the Drude-Lorentz model. The only considerable deviation occurs in the reflection spectra near the onset for interband transitions. The fitting procedure provides, in addition to the fitting parameters in Eq. (1), the layer thickness for each ScN sample. The obtained ScN layer thicknesses are in excellent agreement with the values from SEM analyses for all samples, with the largest deviation in thickness being 6%. Moreover, the optical fitting provides the refractive index $n$ in the transparent photon energy range. It increases from $n$ = 2.6 to 2.8 to 3.1 at h$\nu$ = 1.0, 1.5, and 2.0 eV, respectively, which is in good agreement with the corresponding values of 2.8, 2.9, and 3.2 obtained from the first-principles simulations. The complete data set of the ScN refractive index is included as supplemental material.[75]

Equation (2) is also used to determine the electron transport effective mass $m_{tr}$ at the conduction band bottom at the X-point, which is a fundamental property that controls electron

transport of n-type ScN. For this purpose, we define the optical carrier density $N_{Optic} = (m_o/m_{tr})\times N$, which is directly obtained for each ScN sample from the optical fitting, and is plotted in Fig. 3 vs the carrier concentration $N$ measured by the Hall experiment. The data points are well described by a linear relationship, as indicated by the dashed line drawn from the origin. The slope of 2.5±0.1 corresponds to the ratio $m_o/m_{tr}$, and therefore yields a value for the ScN electron effective mass $m_{tr} = 0.40\pm0.02\ m_o$. This value is in good agreement with $m_{tr} = 0.33\pm0.05\ m_o$ from our first-principles calculations presented above, but is considerably larger than the range $m_{tr} = 0.1\text{-}0.2\ m_o$ reported by Harbeke *et al.* for early work on polycrystalline ScN.[39]

Figure 4 illustrates how the optical properties and particularly the measured direct bandgap are affected by the carrier concentration. We reiterate here, as discussed in Section 2.B., that the carrier concentration, which is primarily controlled by the F doping concentration, is the only detectable parameter affecting the measured optical properties, while varying the nitrogen vacancy concentration and the crystalline quality by the deposition temperature, the ion irradiation energy, and the processing gas composition and pressure, have negligible effect on the ScN optical properties. The plot in Fig. 4(a) shows the optical absorption coefficient $\alpha$, as determined from the measured $R$ and $T$ spectra, using the method from Ref. 42 and the layer thicknesses from the optical fitting described above. As the carrier concentration increases from $N = 1.12$ (black solid line) to 12.8 (pink short-dashed line) $\times10^{20}$ cm$^{-3}$, the free carrier absorption below 1.2 eV increases continuously, from $\alpha < 4\times10^3$ cm$^{-1}$ to $\alpha = 6\times10^4$ cm$^{-1}$ at 0.75 eV. Simultaneously, the onset of strong absorption due to interband transitions above h$\nu$ = 2 eV shifts to higher energies, as evident from the set of nearly parallel $\alpha$-curves, which shift by 0.45 eV for $N = 1.12\text{-}12.8\times10^{20}$ cm$^{-3}$ at the level of $\alpha = 1.5\times10^5$ cm$^{-1}$. Figure 4(a) also shows the $\alpha$-curve predicted for intrinsic ScN ($N = 0$) from the calculated complex dielectric function shown in Fig. 1(b). The simulated absorption onset is at slightly lower photon energies than for the sample with the lowest $N = 1.12\times10^{20}$ cm$^{-3}$, continuing the trend of decreasing onset energy with decreasing $N$. At large absorption, the simulated $\alpha$ values are approximately 25% lower than measured, which may be associated with optical losses for these experiments where only a small fraction ($T < 0.001$) of incident light is

transmitted through the sample, resulting in relatively large systematic experimental uncertainties related to the difficulty in correct calibration at low intensities. Nevertheless, experiment and simulation show good qualitative agreement in both, the onset of optical absorption above 2.0 eV and a reduction in the slope $d\alpha/d(h\nu)$ which is associated with a plateau in $\varepsilon_2$ for $h\nu > 2.5$ eV. This latter feature is observed in the measured $\alpha$ for $N \leq 5.10\times10^{20}$ cm$^{-3}$, but disappears for higher carrier concentrations since electrons fill states in the conduction band and change the absorption profile.

We use the measured $\alpha$ to determine the direct optical bandgap $E_g$ by extrapolating the linear curve in Tauc's plot,[87] $(\alpha h\nu)^2$ vs. $h\nu$, to intersect with the x-axis, as illustrated in the inset of Fig. 4(b) for $N = 8.56\times10^{20}$ cm$^{-3}$. The obtained $E_g$ values from all 19 ScN samples are plotted in Fig. 4(b) as a function of $N$, indicating that $E_g$ increases from 2.18 eV for $N = 1.12\times10^{20}$ cm$^{-3}$ to 2.70 eV for $N = 12.8\times10^{20}$ cm$^{-3}$. This increase is approximately linear, as indicated by the solid line in Fig. 4(b) which is obtained from a linear fit through the measured data. Extrapolation of the linear trend to $N = 0$ yields a bandgap value for carrier-free ScN of $E_{g0} = 2.13\pm0.02$ eV. This value corresponds to the gap of intrinsic ScN, under the assumption that donor impurities have a negligible effect on the shape of the conduction band. This assumption is supported by previously reported calculations showing a nearly identical density of states for $Sc(N_{0.97}F_{0.03})$ and ScN.[29] The value $E_{g0} = 2.13$ eV from linear extrapolation is slightly larger than 2.02 eV, the corresponding value for the direct transition at the X-point obtained from our first-principles calculations using the HSE06 functional presented in Fig. 1(a).

We note, however, that an ideal Burstein-Moss shift assuming parabolic bands should not result in a linear $E_g$ vs. $N$ relationship, but instead in:[53]

$$E_g = E_{g0} + \frac{\pi^{4/3}\hbar^2}{2m_{DOS}} N^{2/3} \tag{3}$$

where $m_{DOS}$ is the density of states (DOS) effective mass at the conduction band bottom. This relationship assumes a flat valence band which is valid in our situation since, as shown in Fig. 1(a), the valence band near the X-point is flat in the X→Γ direction and, as the free carriers fill the conduction band at the X-point, the minimum-energy direct inter-band transition moves along the X→Γ direction.

We also note that the last term in Eq. (3) is a factor $3^{2/3}$ smaller than in the corresponding expression for a zone-center transition, because there are six equivalent X-points at the Brillouin zone boundary such that the Fermi surface of n-type ScN consists of six ellipsoids of which half of each lay inside the first Brillouin zone. We use Eq. (3) to fit the measured $E_g$ data, as illustrated as black dashed line in Fig. 4(b). This provides values for $E_{g0}$ = 2.02±0.03 eV and $m_{DOS}$ = 0.33±0.02 $m_o$, which can be directly compared to, and are in good agreement with, our first-principles predictions of the direct transition energy and $m_{DOS}$ at the X-point of 2.02 eV and 0.43±0.05 $m_o$, respectively. We note, however, that the ideal Burstein-Moss formula, which is the basis for Eq. (3), does not include band-narrowing effects caused by impurities.[53, 88] In addition, the curvature of the dashed line in Fig. 4(b) is not supported by the experimental data which is slightly better described by the linear relationship. Consequently, it is unclear if extrapolation with Eq. (3) yields a more accurate value of $E_{g0}$ than the simple linear relationship. Therefore, we conclude that our experimental value for the direct transition at the X-point is inbetween the two extrapolated values of 2.02 and 2.13 eV, yielding $E_{g0}$ = 2.07±0.05 eV.

In summary, the optical analyses provide values for extrapolated intrinsic ScN of 2.07±0.05 eV for the direct transition at the X-point and 3.80±0.02 eV for a reflection peak associated with a high joint-density of states near the Γ-point. These values are in excellent agreement with our first-principles calculations using the HSE06 hybrid functional which predict corresponding values of 2.02 and 3.79 eV. This suggests that the calculated band structure of ScN is accurate, with an estimated uncertainty of ±0.05 eV in relative band positions. In addition, the band structure is validated by the good agreement between experiment and calculation in the values for the electron effective mass and the absolute magnitude of the dielectric function, as evidenced by the refractive index and the total reflection below and above the onset of interband transitions, respectively. Therefore, based on our calculated electronic structure that is confirmed by optical measurements, we conclude that the indirect Γ to X band gap of ScN is 0.92±0.05 eV. This is at the low end of previously reported values, which range from 0.9-1.5 eV from experimental studies[26, 42, 46, 52] and 0.79-1.70 eV from theoretical investigations that go beyond the conventional local density or generalized gradient approximations.[29,

[42, 54-62] Similarly, our value of 2.07±0.05 eV for the direct transition at the X-point is at the low end of reported measured values of the direct transition determined from optical absorption, ranging from 2.03 to 3.2 eV.[2, 26, 34, 37, 40, 42-48] We note that our samples, similar to the published literature, also yield quite a large range of measured optical gaps, from 2.18 to 2.70 eV. Our data clearly shows that this range is due to a varying carrier concentration and the resulting Burstein-Moss shift. Correspondingly, we attribute the large variation in reported gap values to differences in the carrier concentration of ScN obtained using different synthesis methods. Since the carrier concentration leads to an increase in the apparent band gap, the lowest published values of 2.03 eV are close to the value for intrinsic ScN of 2.07±0.05 eV (from this study) for the direct transition at the X-point.

Figure 5(a) shows the measured electrical resistivity $\rho$ from three typical ScN layers with carrier concentrations of $N$ = 1.12, 5.1, and 10.4×$10^{20}$ $cm^{-3}$. Their residual resistivity at 4 K decreases with increasing carrier concentration from $\rho_o$ = 437 to 173 to 46 μΩ-cm for $N$ = 1.12, 5.1 and 10.4×$10^{20}$ $cm^{-3}$, respectively. These values yield a low-temperature electron mobility of 128, 71, and 131 $cm^2$/Vs, respectively, which is controlled by electron scattering by crystal defects and donor impurities. All samples exhibit a metallic temperature dependence of $\rho$, with a constant low-temperature resistivity and a positive temperature coefficient at higher temperatures. The constant resistivity at low temperature suggests the absence of any thermally-activated transport mechanism that would be expected in a non-degenerate semiconductor or for hopping conduction.[89] That is, all ScN layers in this study are degenerate, with the Fermi level above the disorder induced band tail.[90, 91] This is also confirmed by temperature-dependent Hall measurements (not shown) on the sample with the lowest carrier density, showing that the carrier concentration remains unchanged (±4%) over the entire measured temperature range of 125-350 K, while the carrier mobility decreases by 27% over the same temperature range, consistent with the increase in $\rho$ in Fig. 5(a).

We attribute the increase in resistivity with temperature primarily to polar optical phonon scattering, similar to what has been observed in III-V materials.[92-94] Howarth and Sondheimer have solved the Boltzmann transport equation for the case of highly degenerate semiconductors with

electron scattering at polar optical phonons, and provided an approximate resistivity vs. temperature relationship:[95]

$$\rho(T) = \rho_o + \frac{A}{T(e^{\Theta/T} + e^{-\Theta/T} - 2)} \quad (4)$$

where $\rho_o$ is the residual resistivity, $\Theta = \hbar\omega/k_B$ is the characteristic temperature corresponding to an optical phonon with frequency $\omega$, and $A$ is a prefactor that depends on the dielectric constant, $\Theta$, and the Fermi energy. Other temperature-dependent scattering mechanisms such as acoustic phonon scattering and ionized impurity scattering are neglected because they are expected to have a considerably smaller effect on the resistivity in comparison to polar optical phonon scattering.[95] Equation (4) is used for data fitting of the experimental curves. The resulting curves are plotted as dashed lines in Fig. 5(a), which are nearly indistinguishable from the measured data. The $\Theta$ values obtained from this fitting are plotted in Fig. 5(b) as a function of carrier density. The right axis indicates the corresponding optical phonon vibrational frequency $\omega$ in units of $cm^{-1}$. The ScN layer with the lowest carrier density $N = 1.12\times10^{20}$ $cm^{-3}$ has a $\Theta = 893$ K, corresponding to a phonon frequency of 620 $cm^{-1}$. This is very close to 632 $cm^{-1}$, the previously predicted ScN longitudinal optical (LO) phonon frequency at the zone center.[96] The reported experimental value for the LO phonon mode from Raman scattering is 680 $cm^{-1}$,[34, 97] which is a slightly larger value and can be explained by disorder which allow Raman intensity from LO modes away from the zone center, corresponding to higher frequencies, as previously predicted.[96, 97] The good agreement between the reported LO frequency with the phonon frequency of 620 $cm^{-1}$ from the ScN layer with $N = 1.12\times10^{20}$ $cm^{-3}$ indicates that electron scattering in this layer is dominated by the macroscopic dipole polarization formed by LO phonons. As $N$ increases to 2.04, 2.75, and $5.1\times10^{20}$ $cm^{-3}$, the characteristic phonon temperature $\Theta$ decreases to 791, 764, and 710 K, respectively. At higher $N$, the decrease becomes more moderate suggesting that $\Theta$ may approach a saturation value between 600 and 670 K, corresponding to $\omega = 440\pm30$ $cm^{-1}$. This value is only 20% larger than the predicted transverse optical (TO) phonon mode at the zone center of 365 $cm^{-1}$,[96] while the reported ScN TO frequency from Raman scattering

(likely again not from the zone center) is 420 $cm^{-1}$.[34, 97] Therefore, we attribute the decrease in $\Theta$ to free carrier screening effects that reduce the anion-cation Coulomb interaction and therefore lower the LO phonon vibrational frequency, consistent with the reported comparison of the phonon dispersion curves of TiN and ScN, where the screening from the extra electrons in TiN almost completely cancel LO-TO frequency splitting.[97]

## IV. CONCLUSIONS

Optical and electronic transport measurements on single crystal ScN(001) layers, in combination with first principles density functional calculations, were done with the primary goal to determine the band gaps of ScN as well as its electron effective mass. Experimental parameters during sputter deposition including substrate temperature, ion irradiation energy, nitrogen and argon partial pressures, and power on the Sc target affect the crystalline quality, nitrogen vacancy concentration, and strain in the deposited ScN layers, but have negligible effect on the measured optical properties and particularly the optical interband transition energies. In contrast, a fluorine impurity in the Sc target leads to fluorine doping in the ScN layers and an n-type carrier concentration which varies by an order of magnitude, from $N$ = 1.12-12.8×$10^{20}$ $cm^{-3}$. This carrier concentration strongly affects optical intra and interband transitions. In particular, the optical absorption onset associated with a direct transition at the X-point increases from 2.18 to 2.70 eV as $N$ increases from 1.12-12.8×$10^{20}$ $cm^{-3}$, which is attributed to a Burstein-Moss shift. Extrapolation to $N$ = 0 leads to a direct transition energy at the X-point of 2.13±0.02 or 2.02±0.03 eV, depending on the functional form of the extrapolation, with an overall experimental value for the direct transition of intrinsic ScN of 2.07±0.05 eV. In contrast, higher energy optical transitions near the zone center are unaffected by $N$, resulting in a peak in the reflection spectra for all samples at 3.80±0.02 eV. Temperature dependent resistivity and Hall measurements indicate that all ScN layers are degenerate semiconductors with a negligible temperature dependence in $N$, a low temperature mobility of 100±30 $cm^2$/Vs and a metallic transport with a positive temperature coefficient that is well described by electron scattering at polar optical phonons which have a

frequency that decreases with increasing $N$ due to free carrier screening of the ionic Coulomb interaction, leading to a decrease in the characteristic phonon temperature from 900 to 600 K approximately corresponding to previously reported ScN LO and TO frequencies, respectively.

Electronic structure calculations using a hybrid HSE06 exchange correlation functional indicate that ScN is a semiconductor with a 0.92 eV indirect gap from the Γ-point in the valence band to the X-point in the conduction band, a lowest energy direct transition at the X-point of 2.02 eV and a 3.75 eV gap at the Γ-point. Conventional exchange correlation functionals lead to 1.0 eV lower gap energies, while $G_oW_o$ and $GW_o$ calculations suggest gap values that are 0.44-0.74 eV higher than the hybrid functional values. Comparing predicted optical properties with experiment indicates that the hybrid functional calculations agree closest with experiment. In particular, the predicted direct gap at the X-point is just 0.05 eV below the experimental 2.07±0.05 eV, and the predicted reflection peak at 3.79 eV is in perfect agreement with the experimental 3.80±0.02 eV. This agreement suggests an accuracy of the calculated interband transition energies of ±0.05 eV, such that we conclude that the fundamental indirect gap of ScN is 0.92±0.05 eV. In addition, the first principles calculated electronic structure also agrees in other aspects with the experimental measurements: (i) The transport effective mass calculated from the 3D-curvature of the conduction band bottom at the X-point is 0.33±0.05 $m_0$, in good agreement with $m_{tr}$ = 0.40±0.02 $m_0$ determined from fitting the free carrier contribution to the optical transmission and reflection spectra. (ii) Similarly, the predicted DOS effective mass of 0.43±0.05 $m_o$ agrees reasonably well with the experimental $m_{DOS}$ = 0.33±0.02 $m_o$ obtained by fitting the measured Burstein-Moss shift vs $N$ obtained from Hall measurements. (iii) In addition, the refractive index below the onset of interband transitions is predicted to increase from 2.8 to 3.2 for hν = 1.0-2.0 eV, in good agreement with the experimental values of $n$ = 2.6-3.1, obtained from interference fringes in transmission and reflection spectra.

ACKNOWLEDGEMENTS

This research is supported by NSF through grant Nos. 1309490, 1234872, and 1234777. The authors would like to thank Swatilekha Saha and Prof. Kim M. Lewis for setting up temperature-dependent resistivity measurements, and Rajendra P. Dahal and Prof. Ishwara B. Bhat for help with temperature-dependent Hall measurements. We also acknowledge computational resources provided by the Computational Center for Nanotechnology Innovations (CCNI) at Rensselaer.

## References


[1] C. T. Horovitz, K. A. Gschneidner Jr., G. A. Melson, D. H. Youngblood, and H. H. Schock, *Scandium Its Occurrence, Chemistry Physics, Metallurgy, Biology and Technology* (Academic Press, London, 1975).

[2] D. Gall, I. Petrov, N. Hellgren, L. Hultman, J. E. Sundgren, and J. E. Greene, J. Appl. Phys. **84**, 6034 (1998).

[3] D. Gall, I. Petrov, L. D. Madsen, J. E. Sundgren, and J. E. Greene, J. Vac. Sci. Technol. A-Vac. Surf. Films **16**, 2411 (1998).

[4] Z. T. Y. Liu, X. Zhou, S. V. Khare, and D. Gall, Journal of Physics: Condensed Matter **26**, 025404 (2014).

[5] S. W. King, R. J. Nemanich, and R. F. Davis, Appl. Phys. Lett. **105**, 081606 (2014).

[6] M. A. Moram, M. J. Kappers, T. B. Joyce, P. R. Chalker, Z. H. Barber, and C. J. Humphreys, J. Cryst. Growth **308**, 302 (2007).

[7] M. A. Moram, Y. Zhang, M. J. Kappers, Z. H. Barber, and C. J. Humphreys, Appl. Phys. Lett. **91**, 152101 (2007).

[8] M. A. Moram, C. F. Johnston, M. J. Kappers, and C. J. Humphreys, J. Cryst. Growth **311**, 3239 (2009).

[9] S. M. Knoll, S. K. Rhode, S. Zhang, T. B. Joyce, and M. A. Moram, Appl. Phys. Lett. **104**, 101906 (2014).

[10] M. E. Little and M. E. Kordesch, Appl. Phys. Lett. **78**, 2891 (2001).

[11] C. Constantin, H. Al-Brithen, M. B. Haider, D. Ingram, and A. R. Smith, Phys. Rev. B **70**, 193309 (2004).

[12] R. P. Deng, K. Jiang, and D. Gall, J. Appl. Phys. **115**, 013506 (2014).

[13] M. Akiyama, T. Kamohara, K. Kano, A. Teshigahara, Y. Takeuchi, and N. Kawahara, Advanced Materials **21**, 593 (2009).

[14] R. Deng, S. R. Evans, and D. Gall, Appl. Phys. Lett. **102**, 112103 (2013).

[15] M. Moreira, J. Bjurstrom, I. Katardjev, and V. Yantchev, Vacuum **86**, 23 (2011).

[16] G. Wingqvist, F. Tasnadi, A. Zukauskaite, J. Birch, H. Arwin, and L. Hultman, Applied Physics Letters **97**, 3 (2010).

[17] R. Matloub, A. Artieda, C. Sandu, E. Milyutin, and P. Muralt, Applied Physics Letters **99**, 3 (2011).

[18] R. Matloub, M. Hadad, A. Mazzalai, N. Chidambaram, G. Moulard, C. S. Sandu, T. Metzger, and P. Muralt, Appl. Phys. Lett. **102**, 152903 (2013).

[19] C. Hoglund, J. Birch, B. Alling, J. Bareno, Z. Czigany, P. O. A. Persson, G. Wingqvist, A. Zukauskaite, and L. Hultman, J. Appl. Phys. **107**, 123515 (2010).

[20] C. Ho□glund, J. Bareño, J. Birch, B. Alling, Z. Czigány, and L. Hultman, J. Appl. Phys. **105**, 113517 (2009).

[21] R. Mohammad and S. Katircioglu, International Journal of Modern Physics C **24**, 1350074 (2013).

[22] K. Suzuki, T. Kaneko, H. Yoshida, Y. Obi, H. Fujimori, and H. Morita, Journal of Alloys and Compounds **306**, 66 (2000).

[23] A. Herwadkar and W. R. L. Lambrecht, Phys. Rev. B **72**, 235207 (2005).

[24] A. Herwadkar, W. R. L. Lambrecht, and M. van Schilfgaarde, Phys. Rev. B **77**, 134433 (2008).

[25] H. A. Al-Brithen, H. Q. Yang, and A. R. Smith, J. Appl. Phys. **96**, 3787 (2004).

[26] B. Saha, G. Naik, V. P. Drachev, A. Boltasseva, E. E. Marinero, and T. D. Sands, J. Appl. Phys. **114**, 063519 (2013).

[27] A. Alsaad and A. Ahmad, Eur. Phys. J. B **54**, 151 (2006).

[28] S. Kerdsongpanya, et al., Appl. Phys. Lett. **99**, 232113 (2011).

[29] S. Kerdsongpanya, B. Alling, and P. Eklund, Phys. Rev. B **86**, 195140 (2012).

[30] S. Kerdsongpanya, B. Alling, and P. Eklund, J. Appl. Phys. **114**, 073512 (2013).

[31] P. V. Burmistrova, J. Maassen, T. Favaloro, B. Saha, S. Salamat, Y. R. Koh, M. S. Lundstrom, A. Shakouri, and T. D. Sands, J. Appl. Phys. **113**, 153704 (2013).

[32] A. Neckel, P. Rastl, R. Eibler, P. Weinberger, and K. Schwarz, Journal of Physics C-Solid State Physics **9**, 579 (1976).

[33] R. Monnier, J. Rhyner, T. M. Rice, and D. D. Koelling, Phys. Rev. B **31**, 5554 (1985).

[34] G. Travaglini, F. Marabelli, R. Monnier, E. Kaldis, and P. Wachter, Phys. Rev. B **34**, 3876 (1986).

[35] N. Sclar, J. Appl. Phys. **33**, 2999 (1962).

[36] N. Sclar, J. Appl. Phys. **35**, 1534 (1964).

[37] J. P. Dismukes, W. M. Yim, and V. S. Ban, J. Cryst. Growth **13**, 365 (1971).

[38] J. P. Dismukes, W. M. Yim, J. J. Tietjen, and R. E. Novak, J. Cryst. Growth **9**, 295 (1971).

[39] G. Harbeke, E. Meier, and J. P. Dismukes, Optics Communications **4**, (1972).

[40] E. Kaldis and C. Zurcher, Helvetica Physica Acta **47**, 421 (1974).

[41] D. Gall, I. Petrov, L. D. Madsen, J. E. Sundgren, and J. E. Greene, Journal of Vacuum Science & Technology a-Vacuum Surfaces and Films **16**, (1998).

[42] D. Gall, M. Stadele, K. Jarrendahl, I. Petrov, P. Desjardins, R. T. Haasch, T. Y. Lee, and J. E. Greene, Physical Review B **63**, 9 125119 (2001).

[43] A. R. Smith, H. A. H. Al-Brithen, D. C. Ingram, and D. Gall, J. Appl. Phys. **90**, 1809 (2001).

[44] X. W. Bai and M. E. Kordesch, Applied Surface Science **175**, 499 (2001).

[45] M. A. Moram, Z. H. Barber, and C. J. Humphreys, Thin Solid Films **516**, 8569 (2008).

[46] H. A. Al-Brithen, A. R. Smith, and D. Gall, Phys. Rev. B **70**, 045303 (2004).

[47] T. D. Moustakas, R. J. Molnar, and J. P. Dismukes, Proceedings of the First Symposium on Iii-V Nitride Materials and Processes **96**, 197 (1996).

[48] Y. Oshima, E. G. Villora, and K. Shimamura, J. Appl. Phys. **115**, 153508 (2014).

[49] D. Gall, I. Petrov, and J. E. Greene, J. Appl. Phys. **89**, 401 (2001).

[50] T. Ohgaki, K. Watanabe, Y. Adachi, I. Sakaguchi, S. Hishita, N. Ohashi, and H. Haneda, J. Appl. Phys. **114**, 093704 (2013).

[51] J. M. Gregoire, S. D. Kirby, G. E. Scopelianos, F. H. Lee, and R. B. Dover, J. Appl. Phys. **104**, 074913 (2008).

[52] S. W. King, R. F. Davis, and R. J. Nemanich, J. Vac. Sci. Technol. A **32**, 061504 (2014).

[53] J. G. Lu, et al., J. Appl. Phys. **101**, 083705 (2007).

[54] C. Stampfl, W. Mannstadt, R. Asahi, and A. J. Freeman, Phys. Rev. B **63**, 155106 (2001).

[55] W. R. L. Lambrecht, Phys. Rev. B **62**, 13538 (2000).

[56] J. Liu, X. B. Li, H. Zhang, W. J. Yin, H. B. Zhang, P. Peng, and L. M. Liu, J. Appl. Phys. **115**, 093504 (2014).

[57] A. Qteish, P. Rinke, M. Scheffler, and J. Neugebauer, Phys. Rev. B **74**, 245208 (2006).

[58] R. Mohammad and S. Katircioglu, Condensed Matter Physics **14**, 23701 (2011).

[59] D. Koller, P. Blaha, and F. Tran, Journal of Physics-Condensed Matter **25**, 435503 (2013).

[60] C. E. Ekuma, D. Bagayoko, M. Jarrell, and J. Moreno, AIP Adv. **2**, 032163 (2012).

[61] M. Betzinger, C. Friedrich, A. Gorling, and S. Blugel, Phys. Rev. B **85**, 245124 (2012).

[62] H. Jiang, R. I. Gomez-Abal, P. Rinke, and M. Scheffler, Phys. Rev. B **82**, 045108 (2010).

[63] F. Aryasetiawan and O. Gunnarsson, Reports on Progress in Physics **61**, 237 (1998).

[64] M. Shishkin, M. Marsman, and G. Kresse, Phys. Rev. Lett. **99**, 246403 (2007).

[65] J. Paier, M. Marsman, K. Hummer, G. Kresse, I. C. Gerber, and J. G. Ángyán, The Journal of Chemical Physics **124**, 154709 (2006).

[66] R. P. Deng, P. Muralt, and D. Gall, Journal of Vacuum Science & Technology A **30**, 9 051501 (2012).

[67] E. D. Palik, *Handbook of Optical Constants of Solids* (Academic Press, San Diego, CA, 1998).

[68] O. S. Heavens, *Optical Properties of Thin Solid Films* (Dover Publications, New York, 1991).

[69] L. J. van der Pauw, Philips Technical Review **20**, (1958).

[70] R. T. Haasch, T.-Y. Lee, D. Gall, J. E. Greene, and I. Petrov, Surface Science Spectra **7**, 178 (2000).

[71] N. Krishnamurthy and C. K. Gupta, *Extractive Metallurgy of Rare Earths* (CRC Press, Florida, 2005).

[72] D. Gall, C.-S. Shin, T. Spila, M. Odén, M. J. H. Senna, J. E. Greene, and I. Petrov, J. Appl. Phys. **91**, 3589 (2002).

[73] C.-S. Shin, Y.-W. Kim, D. Gall, J. E. Greene, and I. Petrov, Thin Solid Films **402**, 172 (2002).

[74] H.-S. Seo, T.-Y. Lee, I. Petrov, J. E. Greene, and D. Gall, J. Appl. Phys. **97**, 083521 (2005).

[75] See Supplemental Material at ... for the complete dataset of ScN optical properties from 0-10 eV, and typical x-ray diffraction results. .

[76] G. Kresse and D. Joubert, Phys. Rev. B **59**, 1758 (1999).

[77] J. P. Perdew, K. Burke, and M. Ernzerhof, Phys. Rev. Lett. **77**, 3865 (1996).

[78] J. Heyd, G. E. Scuseria, and M. Ernzerhof, The Journal of Chemical Physics **124**, 219906 (2006).

[79] M. Shishkin and G. Kresse, Phys. Rev. B **74**, 035101 (2006).

[80] M. Shishkin and G. Kresse, Phys. Rev. B **75**, 235102 (2007).

[81] D. Gall, I. Petrov, P. Desjardins, and J. E. Greene, Journal of Applied Physics **86**, (1999).

[82] M. Gajdoš, K. Hummer, G. Kresse, J. Furthmüller, and F. Bechstedt, Phys. Rev. B **73**, 045112 (2006).

[83] F. Fuchs, J. Furthmüller, F. Bechstedt, M. Shishkin, and G. Kresse, Phys. Rev. B **76**, 115109 (2007).

[84] J. Paier, M. Marsman, K. Hummer, G. Kresse, I. C. Gerber, and J. G. Ángyán, The Journal of Chemical Physics **125**, 249901 (2006).

[85] B. Saha, J. Acharya, T. D. Sands, and U. V. Waghmare, J. Appl. Phys. **107**, 033715 (2010).

[86] C. Jacoboni, *Theory of Electron Transport in Semiconductors - A Pathway from Elementary Physics to Nonequilibrium Green Functinons* (Springer Berlin-Heidelberg, Heidelberg, 2010).

[87] J. Tauc, Grigorov.R, and A. Vancu, Physica Status Solidi **15**, 627 (1966).

[88] K. F. Berggren and B. E. Sernelius, Phys. Rev. B **24**, 1971 (1981).

[89] X. Y. Zhang, J. S. Chawla, B. M. Howe, and D. Gall, Physical Review B **83**, 165205 (2011).

[90] N. F. Mott and E. A. Davis, *Electronic Processes in Non-Crystalline Materials* (Clarendon, Oxford, 1979).

[91] B. I. Shklovskii and A. L. Efros, *Electronic Properties of Doped Semiconductor* (Springer-Verlag, Berlin, 1984).

[92] B. K. Ridley, J. Appl. Phys. **84**, 4020 (1998).

[93] V. W. L. Chin, T. L. Tansley, and T. Ostochan, J. Appl. Phys. **75**, 7365 (1994).

[94] D. C. Look, *Electrical Characterization of GaAs Materials and Devices* (John Wiley & Sons, New York, 1989).

[95] D. J. Howarth and E. H. Sondheimer, Proceedings of the Royal Society of London Series a-Mathematical and Physical Sciences **219**, 53 (1953).

[96] T. R. Paudel and W. R. L. Lambrecht, Phys. Rev. B **79**, 085205 (2009).

[97] D. Gall, M. Stoehr, and J. E. Greene, Phys. Rev. B **64**, 174302 (2001).

**Figure Captions**

Fig. 1: (a) Band structure along high-symmetry directions in the Brillouin zone and (b) real $\varepsilon_1$ and imaginary $\varepsilon_2$ part of the dielectric function of ScN, as determined using density functional calculations with the HSE06 hybrid exchange correlation functional. The numerical values of $\varepsilon_1$ and imaginary $\varepsilon_2$ for h$\nu$ = 0-10 eV are included in this paper as supplemental material.[75]

Fig. 2: (a) Reflection and (b) transmission spectra from three representative 192-262 nm thick ScN/MgO(001) layers with different carrier densities $N = 1.12\times10^{20}$, $5.10\times10^{20}$, and $8.56\times10^{20}$ cm$^{-3}$, as a function of photon energy h$\nu$. The dashed lines indicate the result from optical fitting below the onset of interband transitions. Also included in (a) is the reflectance spectrum predicted from first-principles for intrinsic bulk ScN.

Fig. 3: Optical carrier concentration $N_{\text{Optic}}$ determined from optical curve fitting, vs the carrier concentration $N$ obtained from Hall measurements.

Fig. 4: (a) Optical absorption coefficient α vs photon energy from ScN(001) layers with $N$ = 1.12-$12.8\times10^{20}$ cm$^{-3}$, and corresponding first-principles prediction for intrinsic ScN ($N$ = 0). (b) Optical band gap vs $N$, obtained from the Tauc's plot as illustrated for $N = 8.56\times10^{20}$ cm$^{-3}$ in the inset. Solid and dashed lines are from data fitting using a linear relationship and Eq. (3), respectively.

Fig. 5: (a) Resistivity $\rho$ vs temperature for ScN with $N$ = 1.12, 5.1, and $10.4\times10^{20}$ cm$^{-3}$. Dashed lines are from curve fitting using Eq. (4). (b) Characteristic temperature $\Theta = \hbar\omega/k_B$ of ScN phonons with frequency $\omega$ that dominate electron scattering as a function of carrier concentration $N$.

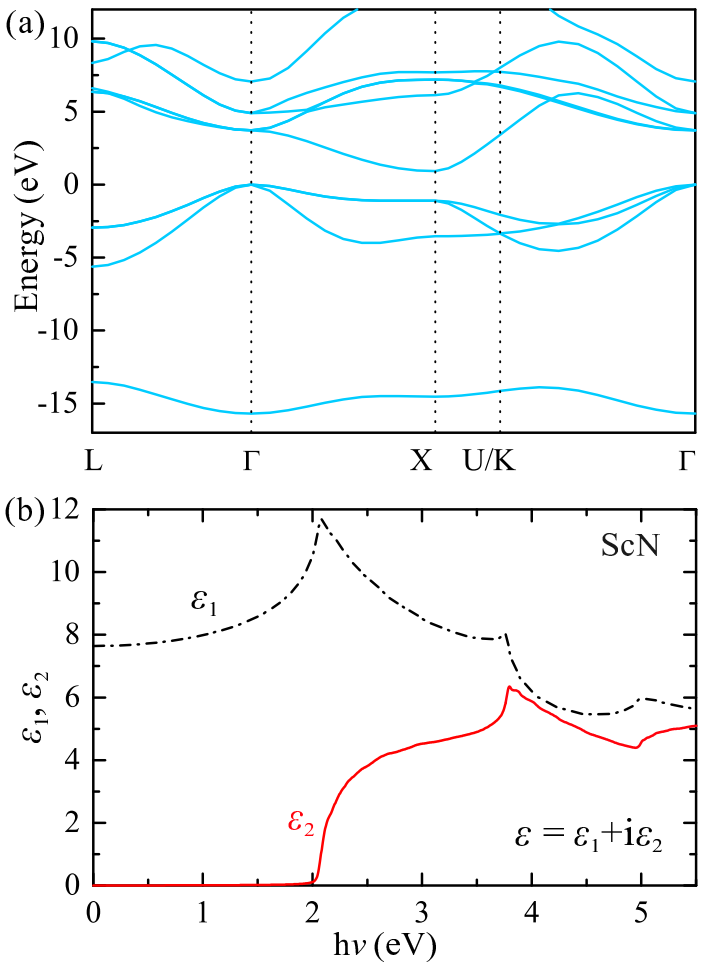


Figure 1 BY12096 11DEC2014

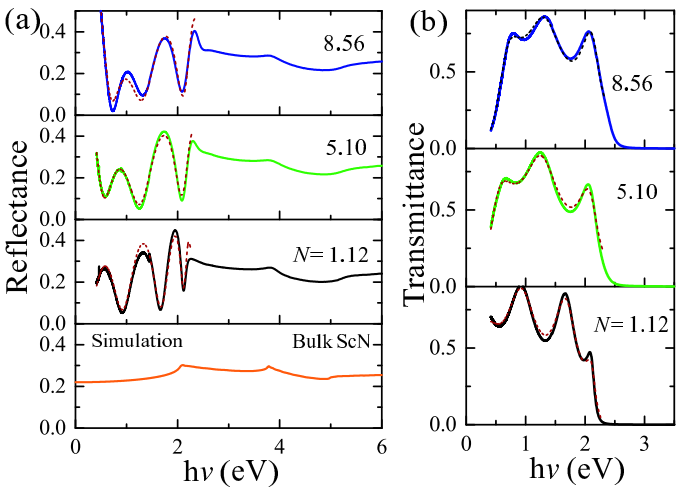


Figure 2 BY12096 11DEC2014

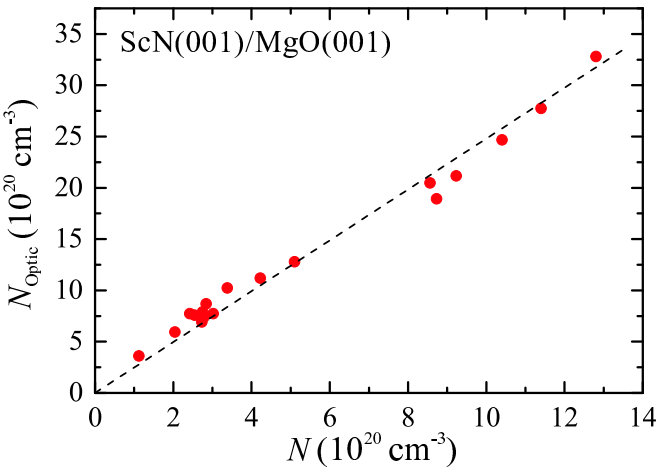


Figure 3 BY12096 11DEC2014

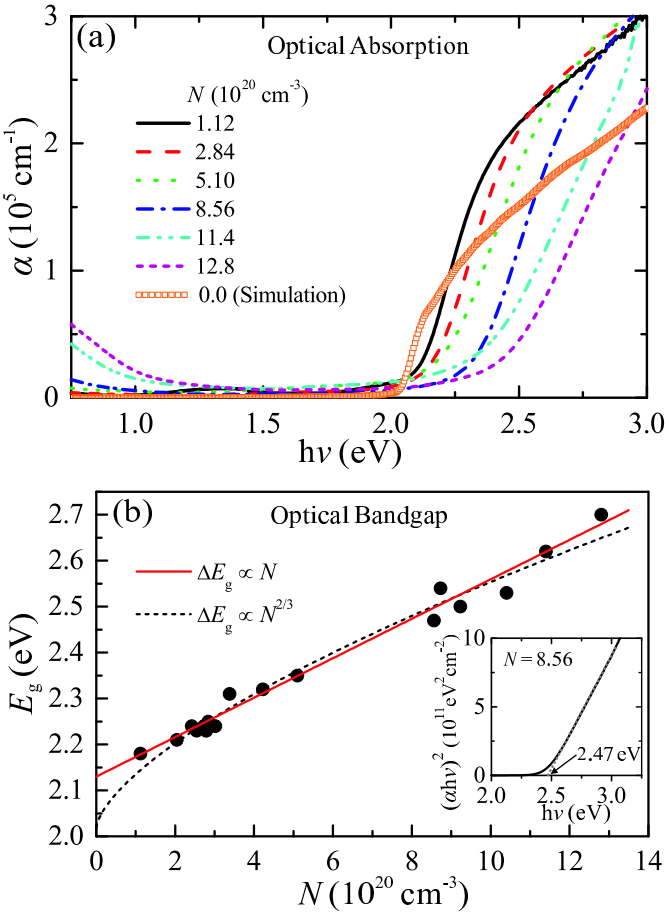


Figure 4 BY12096 11DEC2014

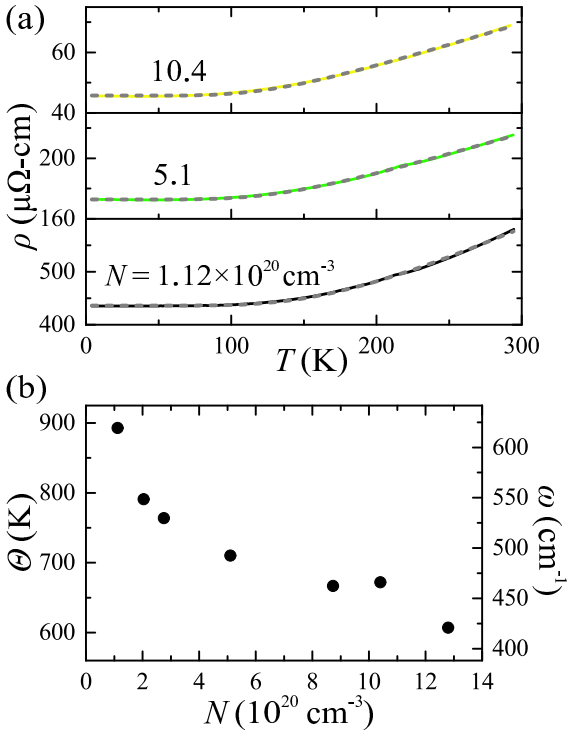


Figure 5 BY12096 11DEC2014